

Optical and Boltzmann conductivities for extrinsic buckled honeycomb lattices at finite temperature

Andrii Iurov^{1*}, Godfrey Gumbs^{2,3}, and Danhong Huang^{4,1}

¹*Center for High Technology Materials, University of New Mexico,
1313 Goddard SE, Albuquerque, NM, 87106, USA*

²*Department of Physics and Astronomy, Hunter College of the City
University of New York, 695 Park Avenue, New York, NY 10065, USA*

³*Donostia International Physics Center (DIPC),
P de Manuel Lardizabal, 4, 20018 San Sebastian, Basque Country, Spain*

⁴*Air Force Research Laboratory, Space Vehicles Directorate, Kirtland Air Force Base, NM 87117, USA*

(Dated: November 27, 2017)

The optical and Boltzmann conductivities have been calculated for doped buckled honeycomb lattice structures such as silicene and germanene, as functions of temperature. By making use of previous results for the temperature-dependent chemical potential for gapped Dirac systems, we have calculated the dynamical polarization function and investigated the way in which initial doping affects its behavior at arbitrary temperature, frequency and wave number. We have calculated the optical and Boltzmann conductivities in the relaxation time approximation. Both these quantities are directly related to the polarizability, with the former being proportional to its long-wavelength limit, whereas the latter depends on static screening and the corresponding dielectric function. We demonstrated that initial doping substantially increases each type of conductivity at intermediate temperatures and we have introduced a formalism for calculating the inverse relaxation time and transition rates for the two inequivalent subbands in silicene.

PACS numbers: 72.10.Fk, 71.45.Gm, 73.20.Mf, 73.21.-b

I. INTRODUCTION

The successful mechanical exfoliation of groups IV and V layered materials has ensured that two-dimensional (2D) materials receive a substantial amount of attention in condensed matter physics. Their planar and buckled structures, lattice asymmetry, nanoscale thickness as well as their stacking arrangements make these 2D materials possess some unusual physical properties and make some of them candidates for device applications. The Hamiltonians used to model these materials need to take account the effect of spin-orbit coupling (SOC), and possible interlayer interactions. While graphene and silicene are two examples of these established 2D materials, sharing many electronic properties of a material having a hexagonal lattice,¹⁻⁴ the silicon-based 2D Kane-Mele topological insulator⁵ possesses a relatively large spin-orbit bandgap ~ 1.55 eV which could be nearly doubled under an applied strain.^{6,7} The band gap arising from sublattice asymmetry leads to an energy bandstructure which is tunable by an external electric field.^{6,8-16} All these effects are due to a finite out-of-plane buckling stemming from a larger ionic radius of silicon compared to carbon and the sp^3 hybridization of electronic orbitals.^{8,12} These properties offer tremendous advantages because electrons could be effectively confined by electrostatic gate voltages yielding potential barriers. Two-dimensional Si-based devices are compatible with standard silicon-based electronics. Compelling experimental evidence for the existence of such graphene-like lattices, for the synthesis of epitaxial silicene sheets on silver, are discussed in Ref. [6].

Other buckled hexagonal 2D lattices include germanene.¹⁷⁻²⁶ Freestanding germanium allotropes had previously been predicted to be stable, low-buckled honeycomb structures with a much larger (~ 23.9 meV) bandgap opened by SOC. Experimentally determined linear V-shaped density-of-states (DOS) serves as a strong verification of a gapped Dirac dispersion relation for germanene.²⁷

There has been a number of key publications on thermal conductivity and transport coefficients for silicene,²⁸⁻³⁰ molecular dynamics studies,³¹ first-principle calculations of electron-phonon coupling and its effect on the electron mobility,³² unusual thermoelectric behavior in Rashba spintronic materials,³³ investigating inhomogeneous quantum critical fluids³⁴ and the effects of anisotropy in phosphorenes³⁵ as well as detailed Monte Carlo studies.³⁶

Boltzmann transport in the presence of scattering by charged impurities has been thoroughly investigated for graphene,³⁷⁻³⁹ finding agreement between theory and existing experimental data.^{40,41} Carrier transport was also investigated in bilayer graphene⁴² and in low-density silicon inversion layers.⁴³ However, the combined effect due to

* Corresponding author's email: aiurov@unm.edu

electron doping and finite temperature on the electron transport in a buckled honeycomb lattices with two diverse energy subbands and gaps, being our principal focus, has not so far received detailed attention.

The rest of the present paper is organized as follows. We briefly introduce the low-energy Hamiltonian, and the electronic states for buckled honeycomb lattices in Sec. II. In Sec. III, we calculate the dynamic polarization function, discuss its behavior for small wave vector and frequencies, which are specifically important for the conductivity calculations. The finite-temperature polarizability depends on the corresponding chemical potential, we provide the existing formalism to obtain $\mu(T)$ for a wide class of gapped Dirac structures with linear DOS. The Optical and Boltzmann conductivity calculations along with the corresponding results are presented in Sec. IV, where we have generalized the existing analytic expression to the case of finite energy bandgaps. We have specifically addressed small, but finite temperatures, for which zero temperature doping is critical. There, we also present and explain our formalism for calculating the inverse relaxation time for elastic transitions in the case of silicene with two different bandgaps, when the transition between such states are possible. Our concluding remarks are provided in Sec. V, where we also briefly discuss how the electron doping affects each type of conductivity for transport.

II. LOW-ENERGY ELECTRONIC STATES AND CHEMICAL POTENTIAL

In this section, we review the existing models for low-energy electronic states and energy bandstructure in buckled honeycomb lattices. Considering silicene as the principal example, we keep in mind that similar properties, i.e., constant internal spin-orbit Δ_{SO} and field-dependent sublattice asymmetry energy $\Delta_z \simeq \mathcal{E}_\perp$ bandgaps and two inequivalent electron subbands could also be attributed to germanene.

The low-energy model Hamiltonian of a buckled honeycomb lattice has been presented in a block-diagonal matrix form as^{8,16}

$$\hat{\mathbb{H}}_{\xi,\sigma} = \begin{pmatrix} -\xi\sigma\Delta_{SO} + \Delta_z & \hbar v_F(k_x - ik_y) \\ \hbar v_F(k_x + ik_y) & \xi\sigma\Delta_{SO} - \Delta_z \end{pmatrix}. \quad (1)$$

Here, $\sigma = \pm 1$ is a real spin index and $\xi = \pm 1$ is a vallet index. The energy dispersion relations are

$$\varepsilon_{\xi,\sigma}^\gamma(k) = \gamma \sqrt{(\xi\sigma\Delta_z - \Delta_{SO})^2 + (\hbar v_F k)^2}, \quad (2)$$

Consequently, we obtain two energy subbands with complete symmetry between electrons and holes. Each subband is specified in Eq. (2) by its own gap $\Delta_{<,>} = |\Delta_{SO} \mp \Delta_z|$, depending only on the product of the valley and spin indices $\beta = \xi \times \sigma$, i.e, they remain the same if both indices are simultaneously changed. This single index β will be widely used throughout this paper.

Both band gaps, $\Delta_\beta = \Delta_{<,>}$, clearly depend on and are determined by the applied electric field \mathcal{E}_\perp , following the corresponding dependence of Δ_z . Once the initially zero field starts to increase, the lower bandgap $\Delta_<$ is decreased, which corresponds to a topological insulator state ($\Delta_z < \Delta_{SO}$, $\Delta_z \geq 0$). When, at some point, the two bandgap values become equal and the lower gap, attributed to a fixed spin index σ in a given valley, is closed. This special and unique state is defined as a valley-spin polarized metal (VSPM)^{8,16}. For all higher electrostatic fields, $\Delta_z > \Delta_{SO}$, representing the standard band-insulator (BI) phase. Finally, $\gamma = \pm 1$ manifests the electron and hole states, in complete analogy with graphene.

In the rest of this paper, energies and frequencies will given in units of a typical Fermi energy $E^{(0)} = 5.22 meV$, which corresponds to an electron density $n^{(0)} = 10^{15} m^{-2}$ for gapless graphene. For many cases, this value will be used as the Fermi energy, unless we include variable doping.

The energy bandstrucutre for silicene in Eq. (2) implies a piecewise linear DOS give by

$$\rho_d(\varepsilon) = \frac{\varepsilon}{\pi (\hbar v_F)^2} \sum_{\gamma=\pm 1} \sum_{\beta=<,>} \Theta\left(\frac{\varepsilon}{\gamma} - \Delta_\beta\right), \quad (3)$$

where $\Theta(x)$ is the Heaviside step function, accounting for the absence of electronic states below the gaps, which is schematically illustrated in Fig. 6 (a). Equation (3) determines the Fermi energy, which is determined by a fixed carrier density n_c at zero temperature as^{44,45}

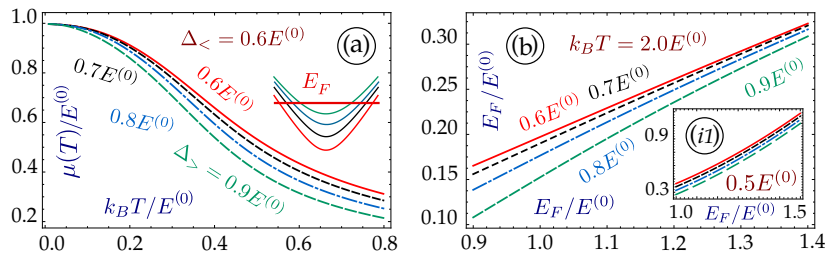


FIG. 1: (Color online) Chemical potential dependence for various temperatures and Fermi energies. Panel (a) shows the temperature dependence of $\mu(T)$ for silicene with $E_F = 1.0 E^{(0)}$ and different bandgaps. While the lower gap is kept $\Delta_{<} = 0.6 E^{(0)}$, the values of $\Delta_{>}$ are varied as $0.6 E^{(0)}$ (gapped graphene, red solid curve), $0.7 E^{(0)}$ (black and short-dashed), $0.8 E^{(0)}$ (blue and dash-dotted) and $0.9 E^{(0)}$ (green and long-dashed line). Plot (b) demonstrates how the chemical potential for silicene with the same bandgaps depends on the Fermi energy (doping at $T = 0$) for $k_B T = 2.0 E^{(0)}$ (the main plot), and for $K_B T = 0.5 E^{(0)}$ at the inset.

$$n_c \cdot 2\pi(\hbar v_F)^2 = \begin{cases} E_F^2 - \Delta_{<}^2 & \text{for } E_F < \Delta_{>} , \\ 2E_F^2 - (\Delta_{<}^2 + \Delta_{>}^2) & \text{for } E_F > \Delta_{>} . \end{cases} \quad (4)$$

The upper subband with gap $\Delta_{>}$ receives doping only if $n_c \geq 2\Delta_{SO}\Delta_z/\pi\hbar^2v_F^2$, which corresponds to the second line of Eq. (4).

The temperature-dependent chemical potential, equal to the Fermi energy at $T = 0$, is obtained using conservation of the carrier density n_c at both zero and finite temperature, which has been discussed in considerable detail in Ref. [44]. It decreases as the temperature is decreased as determined by the following analytic transcendental equation^{44,46,47}

$$n \left(\frac{\hbar v_F}{k_B T} \right)^2 = \sum_{\gamma=\pm 1} \frac{\gamma}{\pi} \sum_{i=<,>} -\text{Li}_2 \left\{ -\exp \left[\frac{\gamma\mu(T) - \Delta_i}{k_B T} \right] \right\} + \frac{\Delta_i}{k_B T} \ln \left\{ 1 + \exp \left[\frac{\gamma\mu(T) - \Delta_i}{k_B T} \right] \right\} , \quad (5)$$

where $\text{Li}_2(x)$ is a polylogarithm function. Once the electron (or hole) density is expressed through the Fermi energy by Eq. (4), the latter quantity is linked to the chemical potential $\mu = \mu(T)$. Specific outcomes for each case are also driven by the energy bandgaps Δ_{β} and, for any given temperature, it depends on the Fermi energy, as described in Fig. 1. Moreover, we observe that such dependence differs at low and intermediate temperatures. In the former case, $k_B T \ll E_F$, Eq. (5) agrees with previously derived approximations.^{48,49}

III. POLARIZATION FUNCTION

We are now positioned to calculate dynamical polarization function $\Pi_{(0)}(q, \omega | \mu, T, \Delta_{\beta})$ for extrinsic silicene at finite temperature. It is one of the most crucial quantities which determines, among others, transport coefficients for an electronic system. We will also need to obtain the dielectric function $\epsilon(q, \omega)$, which in the random phase approximation (RPA) is

$$\epsilon(q, \omega) = 1 - v(q) \Pi_T(q, \omega | \mu, T, \Delta_{\beta}) , \quad (6)$$

where $v(q) = 2\pi e^2/(\epsilon_s q)$ is the Fourier-transformed 2D Coulomb potential, and $\epsilon_s = 4\pi\epsilon_0\epsilon_b$ with ϵ_b denoting the background dielectric constant in which the 2D material is embedded. Zeros of the dielectric function also define the plasmon dispersion relation.^{50,51} For silicene, the plasmons are spin- and valley-polarized and depend on the external electric field,⁵² while the polarization function is a sum¹⁶ of the two corresponding results for gapped graphene⁵¹

$$\Pi^{(0)}(q, \omega | \mu, T) = \sum_{\beta} \Pi^{(0)}(q, \omega | \mu, \Delta_{\beta}) . \quad (7)$$

Both components here depend on a single chemical potential $\mu = \mu(T)$, which is determined from Eq. (5) and depends on each bandgap $\Delta_{<,>}$ individually.

In the one-loop approximation, the dynamical polarization function at both zero and finite temperature is evaluated according to

$$\Pi^{(0)}(q, \omega | E_F, \Delta_\beta) = \frac{1}{4\pi^2} \int d^2k \sum_{\gamma, \gamma' = \pm 1} \mathcal{F}_{\gamma, \gamma'}(\mathbf{k}, \mathbf{q} | \Delta_\beta) \frac{f[\varepsilon_\beta^\gamma(k)] - f[\varepsilon_\beta^\gamma(|\mathbf{k} + \mathbf{q}|)]}{\varepsilon_\beta^\gamma(k) - \varepsilon_\beta^\gamma(|\mathbf{k} + \mathbf{q}|)}. \quad (8)$$

Here, the principal temperature-dependent terms are the Fermi-Dirac distribution functions $f[\mathbb{E}] = f[\varepsilon_\beta^\gamma(k) | \mu(T, E_F), T]$, showing electron and hole occupation numbers for chosen energy \mathbb{E} . At $T = 0$, they are identical to Heaviside unit step functions $\Theta[\mathbb{E} - \varepsilon_\beta^\gamma(k)]$.

The prefactor represents an overlap of the same-subband wavefunctions, corresponding to different wavevectors k and $|\mathbf{k} + \mathbf{q}|$

$$2\mathcal{F}_{\gamma, \gamma'}(\mathbf{k}, \mathbf{q} | \Delta_\beta) = 1 + \gamma\gamma' \frac{\mathbf{k} \cdot (\mathbf{k} + \mathbf{q}) + \Delta_\beta^2}{\varepsilon_\beta^\gamma(k) \varepsilon_\beta^\gamma(|\mathbf{k} + \mathbf{q}|)}. \quad (9)$$

Below, in Sec. IV, we will also derive such an overlap between the electronic states, corresponding to different energy subbands with bandgaps $\Delta_{<, >}$, which play an important role in calculating the Boltzmann conductivity. Any valley or spin transitions are excluded, so that only one index β is used in Eqs. (8) and (7), in contrast to the summation over electron/hole indices γ and γ' .

At arbitrary finite temperature, the dynamical polarization function could also be evaluated as an integral transformation of its zero-temperature value⁵³

$$\Pi^{(0)}(q, \omega | \mu, T) = \frac{1}{2k_B T} \int_0^\infty d\xi \frac{\Pi_0(q, \omega | \xi, \Delta_i)}{1 + \cosh\{[\mu(T, E_F) - \xi]/(k_B T)\}}, \quad (10)$$

where the integration is performed over the Fermi energy for the polarizability at $T = 0$. Using this expression has an obvious advantage compared to a direct calculation by Eq. (8) with finite-temperature distribution functions, because in this case one can use analytic expressions, derived for nearly all 2D Dirac materials at zero temperature.^{16,50,51,54} This integral transformation could be done for all accessible frequency and wave numbers, including the static and long-wavelength limits.

Real and imaginary parts of the polarization function for various gaps, doping levels and temperatures are presented in Figs. 2 and 3. While the dependence on the Fermi energy is a uniform, monotonic increasing function, the gap leads to the decrease of $\Pi^{(0)}$ but its magnitude depends on the frequency and values for the wave vector. Once the temperature is increased, the polarizability is also enhanced, but only for intermediate and high temperatures as can be seen from Fig. 2(c).

IV. TRANSPORT THEORY

We now proceed to calculations of the transport coefficients for extrinsic silicene by making use of our results for the temperature and doping dependent dynamical polarization function. We rely on existing theories to investigate the electronic transport. We mainly focus on (a) the optical conductivity, which depends on the long wavelength limit of the polarizability, and (b) the Boltzmann conductivity, determined by its static limit.

A. Optical conductivity

The optical conductivity, which connects current density to the electric field for various frequencies due to the optically induced electron transitions (mostly direct interband electron transitions in the visible range), is used in calculations of the optical properties of materials in the solid state, such as the transmittance and reflectance. For graphene, such properties were analyzed in the visible and infrared frequency ranges. In the former case, graphene transmittance was demonstrated to be independent of the frequency.⁵⁵⁻⁵⁷ These results were directly supported by measurements of the optical conductivity, reflectivity and transmission for photon energies above 200 meV.⁵⁸

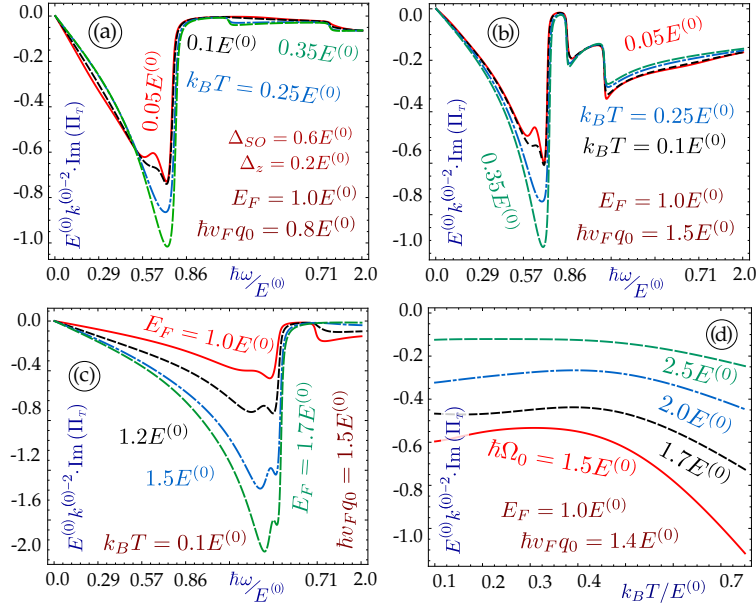


FIG. 2: (Color online) Imaginary part of the dynamical polarization function $\Pi^{(0)}(q, \omega | \Delta_\beta)$, or the single particle excitation spectrum, for silicene with $\Delta_{SO} = 0.6 E^{(0)}$, $\Delta_z = 0.2 E^{(0)}$ and various doping values. Panels (a)-(c) give the frequency dependence of $\text{Im} \Pi^{(0)}(q, \omega | \Delta_\beta)$ for chosen wave vector - $q_0 = 0.8 E^{(0)}/(\hbar v_F)$ for (a) and $1.5 E^{(0)}/(\hbar v_F)$ in (b) and (c). In plots (a) and (b), the red curves correspond to the temperature $0.05 E^{(0)}/k_B$, the black and short-dashed lines to $T = 0.1 E^{(0)}/k_B$, the dotted blue curve to $T = 0.25 E^{(0)}/k_B$ whereas the long-dashed and green curves to $T = 0.35 E^{(0)}/k_B$. Panel (c) presents similar frequency dependence for various doping levels, i.e., the Fermi energies at $T = 0 - 1.0, 1.2, 1.5$ and $1.7 E^{(0)}$. Plot (d) shows the temperature dependence of $\text{Im} \Pi^{(0)}(q, \omega | \Delta_\beta)$ with the same doping values, as those chosen for panel (c).

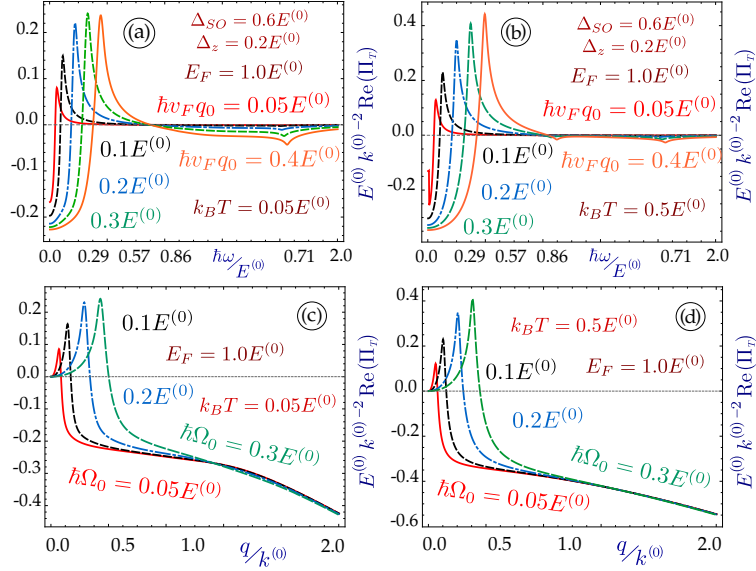


FIG. 3: (Color online) Real part of the dynamical polarization function $\Pi^{(0)}(q, \omega | \Delta_\beta)$ for silicene with $\Delta_{SO} = 0.6 E^{(0)}$, $\Delta_z = 0.2 E^{(0)}$ and Fermi energy $E_F = 1.0 E^{(0)}$. Panels (a) and (b) show the frequency dependence of $\text{Re} \Pi^{(0)}(q, \omega | \Delta_\beta)$ for various wave vectors. We chose $q_0 = 0.05 E^{(0)}/(\hbar v_F)$ is for the red solid curves, $0.1 E^{(0)}/(\hbar v_F)$ for the short-dashed black ones, $0.2 E^{(0)}/(\hbar v_F)$ for the blue dotted, $0.3 E^{(0)}/(\hbar v_F)$ for the long-dashed green, and $0.4 E^{(0)}/(\hbar v_F)$ is given by the solid orange curves. Plots (c) and (d) demonstrate the wave vector dependence of the real part of the polarization for relatively small fixed frequencies, i.e., $\Omega_0 = 0.05 E^{(0)}/\hbar$ (red solid line), $0.1 E^{(0)}/\hbar$ (short-dashed red), $0.2 E^{(0)}/\hbar$ (dash-dotted blue), $0.3 E^{(0)}/\hbar$ (green and long-dashed curve). Panels (a) and (c) correspond to a small temperature $0.05 E^{(0)}/\hbar v_F$, while (b) and (d) to an intermediate value $0.5 E^{(0)}/\hbar v_F$.

The tight-binding calculations of graphene optical conductivity $\sigma_O(\omega)$ based on next nearest neighbor hopping in the visible range showed that the corrections to the Dirac cone approximations are only a few percent,⁵⁹ thereby justifying the validity of the linear subband approximation well above the normally acceptable range of energy. Based on the Dirac cone approximation, we have shown⁶⁰ that induced optical polarization in graphene affects the hybridization of radiative and evanescent fields, which result in localized polarization fields along with modification of an incident surface plasmon-polariton field. Investigation of Dirac quasiparticle transport in the presence of magnetic field in graphene, Hall and optical conductivities was reported in Ref. [61]. A general model for the nonlinear optical conductivity of generic two band systems (gapped or gapless graphene) showed that nonlinearities are controlled by a single dimensionless parameter directly proportional to the incident field strength.⁶²

We present a detailed investigation for arbitrary temperature, doping levels as well as different bandgaps in silicene. As mentioned above, the optical conductivity is directly related to the long wavelength limit of the dynamical polarization function as^{63,64}

$$\sigma_O(\omega | \mu, \Delta_\beta) = ie^2 \lim_{q \rightarrow 0} \frac{\omega}{q^2} \Pi^{(0)}(q, \omega | \mu, \Delta_\beta) \quad (11)$$

But, in the long wavelength limit, the dynamical polarization function behaves like $\sim q^2$ for all 2D systems, regardless of their bandgap⁶⁵, and for all temperatures.^{45,49,66} Such behavior of the electron polarizability leads to the $\sim \sqrt{q}$ plasmon dispersion relation for $q \rightarrow 0$, and only this type of dependence ensures that the optical conductivity is finite.

The polarization function in the long wavelength limit is especially simple at zero temperature given by^{50,51,66}

$$\begin{aligned} \text{Re } \Pi^{(0)}(q, \omega | \Delta_\beta) &= \frac{1}{\pi \hbar} \frac{q^2}{\omega} \sum_{\beta=\pm 1} \left\{ \frac{E_F}{\hbar \omega} \left[1 - \left(\frac{\Delta_\beta}{E_F} \right)^2 \right] + \frac{1}{4} \left[1 + \left(\frac{2\Delta_\beta}{\hbar \omega} \right)^2 \right] \ln \left| \frac{2E_F - \omega}{2E_F + \omega} \right| \right\}, \\ \text{Im } \Pi^{(0)}(q, \omega | \Delta_\beta) &= -\frac{\hbar}{4} \frac{q^2}{\omega} \sum_{\beta=\pm 1} \left\{ \left[1 + \left(\frac{2\Delta_\beta}{\hbar \omega} \right)^2 \right] \Theta \left[\omega - \frac{2E_F}{\hbar} \right] \right\}. \end{aligned} \quad (12)$$

In the real part of $\Pi^{(0)}(q, \omega | \Delta_\beta)$, the second term ($\sim \ln |(2E_F - \omega)/(2E_F + \omega)|$) has negligible effect on the plasmon dispersion relation as a result of the $\omega \ll E_F$ condition. Consequently, it is often omitted which leads to the so-called *absorption threshold* at $\omega_c \sim E_F/2$,⁵⁵⁻⁵⁷ for both zero and finite bandgaps. However, this significantly affects the optical conductivity at finite frequencies.

It is evident from Eq. (11) that the real (imaginary) part of the conductivity is generated by the imaginary (real) part of the dynamical polarization function. Therefore, Eq. (12) leads to the following expressions for the optical conductivity

$$\text{Re } \sigma_O(\omega | E_F, \Delta_\beta) = \frac{e^2}{4\hbar} \sum_{\beta=\pm 1} \left\{ \Theta \left[\omega - \frac{2E_F}{\hbar} \right] \left[1 + \left(\frac{2\Delta_\beta}{\hbar \omega} \right)^2 \right] \right\}, \quad (13)$$

$$\text{Im } \sigma_O(\omega | E_F, \Delta_\beta) = \frac{e^2}{\pi \hbar} \sum_{\beta=\pm 1} \left\{ \frac{E_F}{\hbar \omega} \left[1 - \left(\frac{\Delta_\beta}{E_F} \right)^2 \right] + \frac{1}{4} \left[1 + \left(\frac{2\Delta_\beta}{\hbar \omega} \right)^2 \right] \ln \left| \frac{2E_F - \omega}{2E_F + \omega} \right| \right\}. \quad (14)$$

Here, a step function represents the presence of a conductivity filter which is referred to as a *state-blocking effect*.^{58,61,62} At finite temperature, the step function is modified as follows^{55,59}

$$\Theta \left[\mu(T=0) - \varepsilon_\beta^\gamma(k) \right] \implies \frac{1}{2} \left\{ 1 - \tanh \left[\frac{\varepsilon_\beta^\gamma(k) - \mu(T)}{2k_B T} \right] \right\}, \quad (15)$$

so that this frequency dependence becomes smooth and the conductivity is finite for all accessible frequencies. At finite temperature, the imaginary part is always present which leads to a finite optical conductivity. However, at high temperature, the imaginary part of the polarizability is decreased as $1/T$, so that the effect of temperature depends substantially on the regime and is not uniform.

Making use of Ref. [49], we obtain the optical conductivity for gapless doped graphene in the limit $k_B T \gg E_F$ to be

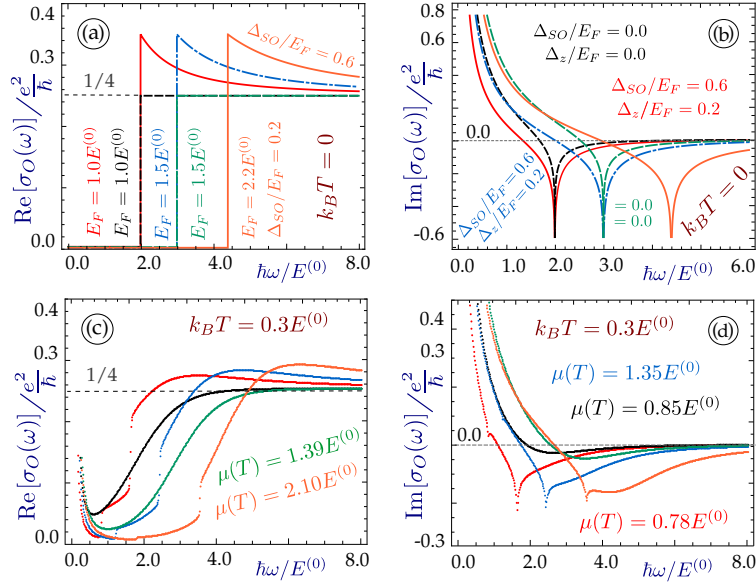


FIG. 4: (Color online) Optical conductivity of silicene at zero and low temperatures. Left panels (a) and (c) show the real part of $\sigma_O(\omega | \mu(E_F, T), \Delta_\beta, T)$, and the ones on the right-hand side in (b) and (d) give its imaginary part. In all plots, each curve corresponds to chosen values of the energy badgap and Fermi energy - $\Delta_{SO} = 0.6 E^{(0)}$, $\Delta_z = 0.2 E^{(0)}$ and $E_F = 1.0 E^{(0)}$ for the red line, $\Delta_{SO} = \Delta_z = 0.0 E^{(0)}$ and $E_F = 1.0 E^{(0)}$ - for black one, $\Delta_{SO} = 0.6 E_F = 0.9 E^{(0)}$, $\Delta_z = 0.2 E_F = 0.3 E^{(0)}$ and $E_F = 1.5 E^{(0)}$ for the blue, $\Delta_{SO} = \Delta_z = 0.0 E^{(0)}$ and $E_F = 1.5 E^{(0)}$ for green and long-dashed, and $\Delta_{SO} = 0.6 E_F = 1.32 E^{(0)}$, $\Delta_z = 0.2 E_F = 0.44 E^{(0)}$ and $E_F = 2.2 E^{(0)}$ for the orange solid curve. The upper panels (a) and (b) show the situation for zero temperature, while the lower ones ((c) and (d)) - for $k_B T = 0.3 E^{(0)}$.

$$\sigma_O(\omega | E_F, T) \simeq \frac{e^2}{h} \left\{ \frac{1}{16} \frac{\hbar\omega}{k_B T} \left[1 - \frac{1}{3} \left(\frac{\hbar\omega}{4k_B T} \right)^2 \right] + i \frac{2}{\pi} \frac{k_B T}{\hbar\omega} \ln 2 \left[1 + 2 \ln 2 \left(\frac{E_F}{4 \ln 2 k_B T} \right)^4 \right] \right\}. \quad (16)$$

Correction to the imaginary part does not depend on doping, just as we had for the polarization function.

Finally, for intrinsic (undoped) gapped graphene at high temperature, i.e., $T \gg E_F/k_B$

$$\begin{aligned} \text{Re } \sigma_O(\omega, T | E_F, \Delta_0) &= \frac{e^2}{16\hbar} \frac{\hbar\omega}{k_B T} \left(1 - \frac{\Delta_0}{\hbar\omega} \right), \\ \text{Im } \sigma_O(\omega, T | E_F, \Delta_0) &= \frac{4e^2}{\pi\hbar} \frac{k_B T}{\hbar\omega} \left\{ 2 \ln 2 - \left(\frac{\Delta_0}{k_B T} \right)^2 \left[\mathbb{C} - \ln \left(\frac{\Delta_0}{2k_B T} \right) \right] \right\}, \end{aligned} \quad (17)$$

where $\mathbb{C} \simeq 0.79$. It is interesting to note that the real and imaginary parts possess opposite types of dependence on the temperature and frequency. Here, we specifically consider the undoped case so that if $E_F = 0$, $\mu(T) = 0$ for arbitrary T . If the temperature is high, the E_F term is replaced with $k_B T$.

For silicene, with two inequivalent bandgaps, the corresponding result is obtained as a summation over the two bandgaps $\Delta_\beta = \Delta_{>,<}$

$$\sigma_O(\omega, T | \mu) = \sum_{\beta=\pm 1} \sigma(\omega, T | \mu, \Delta_\beta). \quad (18)$$

Only for intermediate temperatures, the optical conductivity cannot be obtained analytically. Our numerical results are presented in Fig. 4.

The real and imaginary parts of $\Pi^{(0)}$ are of course connected by the Kramers-Kronig relations, so that we see such a correspondence between the real and imaginary parts of the conductivity. Namely, the discontinuities of the real part are related to the negative peaks of $\text{Im } \sigma_O(\omega)$. These negative peaks depend on the temperature. However, this

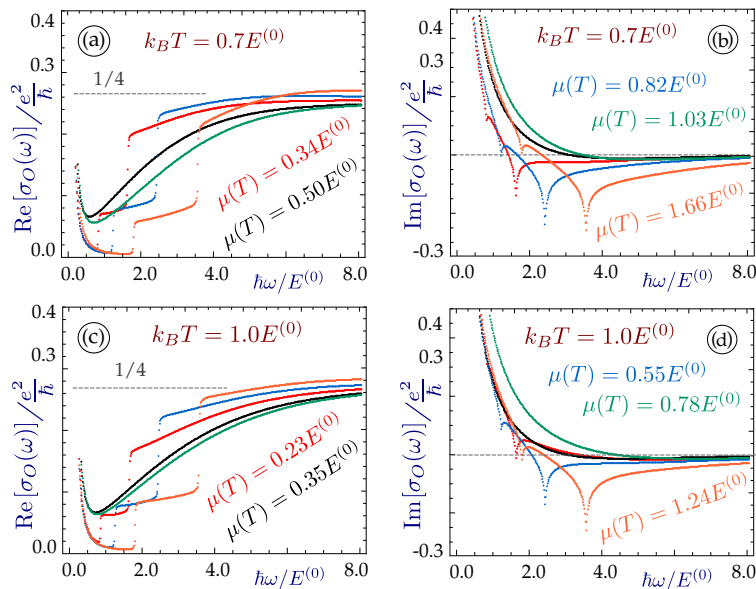


FIG. 5: (Color online) Optical conductivity of silicene at intermediate ($\sim E^{(0)}$) temperatures. Left panels (a) and (c) show the real part of $\sigma(\omega | \mu(E_F, T), \Delta_\beta, T)$, and the right ones (b) and (d) - its imaginary part. In all plots, each curve corresponds to a specific values of the energy badgaps and Fermi energy - $\Delta_{SO} = 0.6 E^{(0)}$, $\Delta_z = 0.2 E^{(0)}$ and $E_F = 1.0 E^{(0)}$ for the red line, $\Delta_{SO} = \Delta_z = 0.0 E^{(0)}$ and $E_F = 1.0 E^{(0)}$ - for black one, $\Delta_{SO} = 0.6 E_F = 0.9 E^{(0)}$, $\Delta_z = 0.2 E_F = 0.3 E^{(0)}$ and $E_F = 1.5 E^{(0)}$ for the blue, $\Delta_{SO} = \Delta_z = 0.0 E^{(0)}$ and $E_F = 1.5 E^{(0)}$ for green and long-dashed, and $\Delta_{SO} = 0.6 E_F = 1.32 E^{(0)}$, $\Delta_z = 0.2 E_F = 0.44 E^{(0)}$ and $E_F = 2.2 E^{(0)}$ for the orange solid curve. The upper panels (a) and (b) show the situation for $k_B T = 0.7 E^{(0)}$, while the lower ones ((c) and (d)) - for $k_B T = 1.0 E^{(0)}$.

connection is not equivalent to that of the chemical potential (see the labels of Figs. 4 and 4). The peaks are observed in the two different boundaries of the interband particle-hole modes for $q \rightarrow 0$, without an obvious relation to the temperature. For $k_B T \gg E_F$, the approximated expression for graphene is $(\omega - 2E_F)^2 \Rightarrow [\omega - 2\mu(T)]^2 + 4T^2$.^{55,57} In some sense, these discontinuities are similar to the static screening results for silicene.¹⁶ But, the analogy is not complete since the latter case corresponds to zero frequency and the boundaries of the interband particle-hole modes, but not the long wavelength limit.

As we see from Fig. 4, at small temperatures, the conductivity behavior is similar to the case for zero-temperature for which the optical conductivity has been obtained analytically based on the corresponding expressions for the polarizability in Ref. [16]. For $k_B T = 0.3 E^{(0)}$, the systems with no bandgap behave in a specific way with the imaginary part showing no negative peaks, and the real part demonstrating a smooth monotonically increasing frequency dependence. Furthermore, there are no discontinuities. (Compare with Eq. (13) for $T = 0$.) Even for an intermediate temperature $k_B T = 1.0 E^{(0)}$, presented in Fig. 5, the two distinct negative peaks of the imaginary part of $\sigma_O(\omega)$ (or jumps of its real part) persist, and the frequency dependence is not yet totally smooth.

B. Boltzmann transport equation

We now turn to our calculation of the Boltzmann conductivity in doped gapped graphene and silicene due to the elastic Coulomb potential scattering from charged impurities as well as the temperature-dependent screening ascribed to the inverse dielectric function $1/\epsilon(q, T)$, with $\epsilon(q, T)$ given in Eq. (6). General theory for the Boltzmann conductivity in graphene, developed in Ref. [48], shows a non-monotonic temperature dependence, which could be affected by a variety of factors. Once the energy gaps are introduced, we also have to deal with a nontrivial dependence on the chemical potential, as shown above in Sec. II.

In Boltzmann theory, the conductivity is given by an average over energy as follows

$$\sigma_B(E_F, T) = -\frac{e^2 v_F^2}{2} \int_0^\infty d\varepsilon \frac{\partial f(\varepsilon)}{\partial \varepsilon} \rho_s(\varepsilon) \tau(\varepsilon). \quad (19)$$

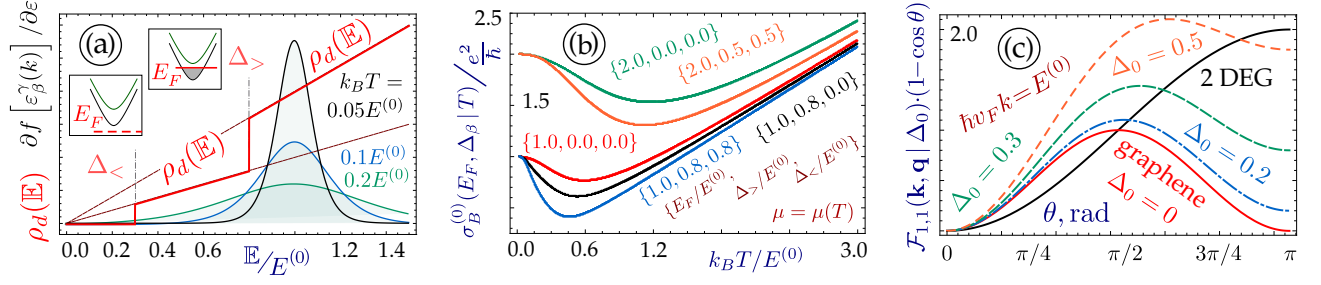


FIG. 6: (Color online) Boltzmann conductivity dependence on the energy bandgap Δ_0 . Panel (a) shows the overlay of the two-step density-of-states $\rho_d(\mathbb{E})$ for silicene with the derivative of the Fermi-Dirac distribution function $\partial [f(\varepsilon_\beta^\gamma(k) - \mu(T))] / \partial \varepsilon$. Plot (b) describes how the angular dependence of the inverse relaxation time, the wave function overlap $\mathcal{F}_{\gamma,\gamma'}(\mathbf{k}, \mathbf{q} | \Delta_0)$ and $(1 - \cos \theta_{k,k'})$ Born scattering term. Panel (c) presents the approximated Boltzmann conductivity with $1/\tau(\varepsilon) = \hbar/E^{(0)}$ for silicene with various gaps and doping values.

For the case of electron doping, $E_F > 0$, integration is carried out over the conduction band energies. At $T = 0$, $-\partial f(\varepsilon)/\partial \varepsilon \implies \delta(\varepsilon - E_F)$ and the Fermi level is always located above the bandgap, i.e. $E_F > \Delta_0$. When the temperature is finite but small with $k_B T \ll E_F$, the derivative of the distribution function could be replaced by a representation of the delta function, so that only a narrow energy range around E_F contributes. In contrast, at high temperature, i.e., $k_B T \gtrsim E_F$, the finite slope for the derivative of the Fermi-Dirac distribution function is spread over all energies $\varepsilon > 0$ and the substantial part of the integral disappears due to the zero density of states in the bandgap region $\varepsilon < \Delta_0$. This situation is illustrated in Fig. 6 (a) for silicene with two inequivalent bandgaps $\Delta_\beta = \Delta_{>,<}$. We see that a finite energy gap always leads to a reduction of the conductivity, however this reduction becomes significant only at high temperature.

An important quantity in our investigation is the average relaxation time $\tau(\varepsilon)$ defined by^{48,67,68}

$$\frac{1}{\tau(\varepsilon)} = \frac{\pi}{\hbar} N^{(i)} \int \frac{d^2 \mathbf{k}'}{(2\pi)^2} \left| \frac{V^{(i)}(q)}{\varepsilon(q, T)} \right|^2 \delta_{\gamma,\gamma'} \delta [\varepsilon_\beta^\gamma(k) - \varepsilon_\beta^\gamma(k')] \mathbb{F}_{\gamma,\gamma'}(\mathbf{k}, \mathbf{q} | \Delta_\beta) (1 - \cos \theta_{\mathbf{k}, \mathbf{k}'}). \quad (20)$$

We note that due to energy conservation only intraband transitions are allowed, i.e., $\gamma = \gamma'$. While the $\sim (1 - \cos \theta_{\mathbf{k}, \mathbf{k}'})$ scattering term remains the same for all sorts of electronic states, the other one represents the Coulomb potential matrix element $\langle \mathbf{k}, \gamma | 2\pi\alpha/q | \mathbf{k} + \mathbf{q}, \gamma' \rangle$. It is given by the wavefunction overlap (9) and, therefore, depends on the energy bandgaps Δ_β . The approximated angular dependence of the inverse relaxation time for a single bandgap $\Delta_0^{(i)}$ and $k = k_0$ is presented at Fig. 6 (b). The results are very different from both the conventional two-dimensional electron gas (2DEG) and gapless monolayer graphene. While the larger values for this dependence are shifted towards larger angles θ , as we had for the 2DEG, they also noticeably exceed the corresponding values for gapless monolayer graphene. Consequently, the relaxation time is decreased, just like the conductivity. This is the second mechanism of the Boltzmann conductivity suppression due to a finite gap Δ_0 .

Specifically, when graphene is irradiated with circularly polarized light,⁶⁹ the created energy gap leads to a smooth monotonic decrease of the conductivity⁷⁰ as $\simeq (16E_F^2 - \Delta_\beta^2)/(16E_F^2 + 3\Delta_\beta^2)$. The reason for this is the decrease of the Fermi velocity

$$\mathcal{V}_F(E_F | \Delta_\beta) = \hbar^{-1} \left| \Delta_{\mathbf{k}} \varepsilon_\beta^\gamma \left(k = k_F^{(\beta)} \right) \right| = \gamma \frac{v_F}{E_F} \sqrt{E_F^2 - \Delta_\beta^2} \Theta[E_F - \Delta_\beta], \quad (21)$$

for chosen Fermi energy E_F , due to the enhanced energy bandgap 2Δ . Here $v_F = \mathcal{V}_F(E_F | 0)$, corresponding to zero bandgap, for the energy dispersions.

Equation (20) could be simplified due to the presence of a delta function. Let us first consider gapped graphene with fourfold-degenerate energy subbands and a single, finite gap Δ_0 . One approach is to the delta function to perform the radial integration, which gives the conductivity due to the screening:

$$\begin{aligned} \frac{1}{\tau(\varepsilon|\Delta_0, T)} &= \frac{2N_i}{\pi\hbar} \frac{[\varepsilon^2 - \Delta_0^2]^{1/2}}{(\hbar v_F)^2} \times \\ &\times \int_0^1 d\xi \frac{\xi^2}{\sqrt{1-\xi^2}} \left\{ 1 + \frac{\Delta_0^2 + [1-2\xi^2](\hbar v_F k)^2}{\Delta_0^2 + (\hbar v_F k)^2} \right\} \left[\frac{k}{\alpha\pi} \xi - \Pi^{(0)}(2k\xi, T|\mu(T), \Delta_0) \right]^{-2}, \end{aligned} \quad (22)$$

where the energy $\varepsilon^{\gamma=1}(k)$ and wave vector k are related by $\varepsilon^{\gamma=1}(k) \Theta(\varepsilon - \Delta_0) = \sqrt{(\hbar v_F k)^2 + \Delta_0^2}$. There is no reason to calculate it in the gap region since the corresponding DOS is zero and it does not contribute to the conductivity integral in Eq. (19). This expression could be obtained by a simple one-step numerical integration.

Alternatively, the inverse relaxation time due to the energy averaging could be determined if the angular integration is done, giving

$$\begin{aligned} \frac{1}{\tau(\varepsilon|\Delta_0, T)} &= \frac{N_i}{\pi\hbar} \frac{\varepsilon}{(\hbar v_F)^2} \int_0^{2k} \frac{dq}{k} \left(\frac{q}{k}\right)^2 \left[1 - \left(\frac{q}{2k}\right)^2 \right]^{-1/2} \times \\ &\times \left\{ 1 + \frac{\Delta_0^2 + (\hbar v_F k)^2 (1 - 2q^2/k^2)}{\Delta_0^2 + (\hbar v_F k)^2} \right\} \left[\frac{q}{2\pi\alpha} - \Pi^{(0)}(q|\mu(T), \Delta_0) \right]^{-2}. \end{aligned} \quad (23)$$

It is important to note that the integral prefactor is $\sim \varepsilon$, and not to $k = \sqrt{\varepsilon^2 - \Delta_0^2}$, as we had in Eq. (22) as a result of the term $k/\sqrt{k^2 + \Delta_0^2}$, which appears from the presence of a delta function.

At $T = 0$, the polarization function for silicene with two different bandgaps $\Delta_\beta = \Delta_{<,>} = |\Delta_{SO} + \beta\Delta_z|$ is given analytically as^{16,51}

$$\Pi^{(0)}(q, T=0|\Delta_\beta) = -\frac{E_F}{\pi} \sum_{\beta=\pm 1} f_{<}(q) \Theta[\Delta_\beta - E_F] + f_{>}(q) \Theta[E_F - \Delta_\beta], \quad (24)$$

and

$$\begin{aligned} f_{<}(q) &= \frac{\Delta_\beta}{2E_F} + \left(\frac{\hbar v_F q}{4E_F} - \frac{\Delta_\beta^2}{4\hbar v_F q E_F} \right) \arcsin \left[1 + \left(\frac{2\Delta_\beta}{\hbar v_F q} \right)^2 \right]^{1/2}, \\ f_{<}(q) &= 1 - \Theta[q - 2k_F^\beta] \left\{ \frac{1}{2} \sqrt{1 - \left(\frac{2k_F^\beta}{q} \right)^2} - \left(\frac{\hbar v_F q}{4E_F} - \frac{\Delta_\beta^2}{4\hbar v_F q E_F} \right) \arctan \frac{\sqrt{q^2 - 4(k_F^\beta)^2}}{2E_F} \right\}. \end{aligned} \quad (25)$$

The two inequivalent Fermi momenta $k_F^{\beta=\pm 1} = \sqrt{E_F^2 - \Delta_\beta^2}$ now depend on the bandgaps Δ_β . For gapped graphene, this result is simplified by the substitution $\Delta_{<,>} = \Delta_0$.

Finally, we consider the case when silicene has two inequivalent gaps $\Delta_{<,>}$. We now need to calculate the wavefunction overlap for two different gaps, which was not encountered in calculating the overlap in Eq. (9). The wavefunction is given by

$$\Psi_\beta^\gamma(k|\Delta_\beta) = \frac{1}{\sqrt{2\mathbb{E}_\beta(k)}} \left[\frac{\sqrt{\mathbb{E}_\beta(k) + \gamma\Delta_\beta}}{\gamma\sqrt{\mathbb{E}_\beta(k) - \gamma\Delta_\beta}} e^{i\phi_{\mathbf{k}}} \right], \quad (26)$$

where $\mathbb{E}_\beta(k) = \varepsilon_\beta^\gamma(k)/\gamma = +\sqrt{(\hbar v_F k)^2 + \Delta_\beta^2}$ is the absolute value of the electron energy independent of the valence or conduction band. It is straightforward to verify that the sought overlap given by

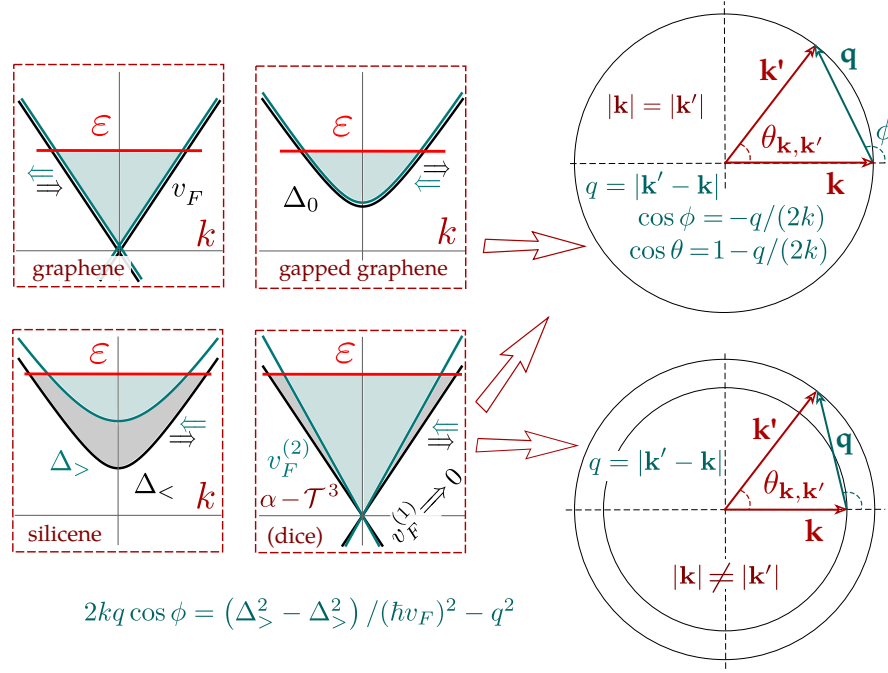


FIG. 7: (Color online) Schematics for allowable wave vectors corresponding to elastic transitions $\varepsilon_{\beta=\pm 1}^{\gamma=1}(\mathbf{k}) = \varepsilon_{\beta=\pm 1}^{\gamma=1}(\mathbf{k}')$ for fourfold-degenerate subbands in graphene with $g_c = g_s g_v = 4$ and partially degenerate subbands in silicene and dice lattices. For the latter case, transitions with different wave vector values $|\mathbf{k}| \neq |\mathbf{k}'|$ are also possible.

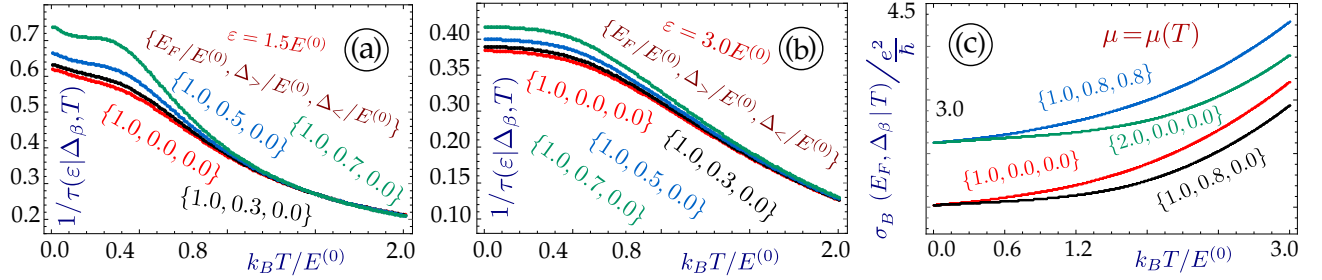


FIG. 8: (Color online) Inverse relaxation time and Boltzmann conductivity for silicene at various temperatures. Plots (a) and (b) present the temperature dependence of $1/\tau(\varepsilon|\Delta_\beta, T)$ for $E_F = 1.0 E^{(0)}$, $\Delta_{>} = \Delta_{<} = 0$ (red line), $E_F = 1.0 E^{(0)}$, $\Delta_{>} = 0.3 E^{(0)}$, $\Delta_{<} = 0$ (black), $E_F = 1.0 E^{(0)}$, $\Delta_{>} = 0.5 E^{(0)}$, $\Delta_{<} = 0$ (blue) and $E_F = 1.0 E^{(0)}$, $\Delta_{>} = 0.7 E^{(0)}$, $\Delta_{<} = 0$ (green). Panel (a) corresponds to $\varepsilon = 1.5 E^{(0)}$, while plot (b) - to $\varepsilon = 3.0 E^{(0)}$. Panel (c) shows the temperature dependence of the Boltzmann conductivity for silicene with $E_F = 1.0 E^{(0)}$, $\Delta_{>} = \Delta_{<} = 0$ (red), $E_F = 1.0 E^{(0)}$, $\Delta_{>} = 0.8 E^{(0)}$, $\Delta_{<} = 0.0 E^{(0)}$ (black), $E_F = 2.0 E^{(0)}$, $\Delta_{>} = \Delta_{<} = 0$ (blue) and $E_F = 2.0 E^{(0)}$, $\Delta_{>} = 1.6 E^{(0)}$, $\Delta_{<} = 0.0 E^{(0)}$ (green line).

$$\mathcal{F}_{\gamma, \gamma'}(\mathbf{k}, \mathbf{q} | \Delta_{1,2}) = \left| \langle \Psi_1^\gamma(k | \Delta_\beta) | \Psi_2^{\gamma'}(k | \Delta_2) \rangle \right|^2 = \frac{1}{2} \left\{ 1 + \gamma\gamma' \frac{\Delta_1 \Delta_2 + k k' \cos \theta_{\mathbf{k}, \mathbf{k}'}}{\mathbb{E}_1(k) \mathbb{E}_2(k')} \right\}, \quad (27)$$

agrees with Eq. (9) when $\Delta_1 = \Delta_2$ and $\mathbb{E}_1(k) = \mathbb{E}_2(k)$. Here, we also used an obvious geometrical relation $k' \cos \theta_{\mathbf{k}, \mathbf{k}'} = k + q \cos \phi$ (see Fig. 7) in order to present the result in terms of the integration variables for Eq. (20):

$$\frac{1}{\tau(\varepsilon|T)} = \frac{1}{4} \sum_{i,j=\langle, >} \frac{1}{\tau(\varepsilon|\Delta_i, \Delta_j, T)} \quad (28)$$

includes transitions for both identical and different bandgaps $\mathbb{E}_i \Rightarrow \mathbb{E}_i$, $\mathbb{E}_i \Rightarrow \mathbb{E}_j$, $\mathbb{E}_j \Rightarrow \mathbb{E}_i$ and $\mathbb{E}_j \Rightarrow \mathbb{E}_j$. For gapped graphene with $\Delta_{<} = \Delta_{>} = \Delta_0$ all four terms become identical and we arrive at Eq. (22).

The allowed values of angle $\phi_{\mathbf{k}}$ are given by the following equation

$$\begin{aligned}\cos \phi_{\mathbf{k}} &= \frac{\Delta_i^2 - \Delta_j^2}{2(\hbar v_F)^2 k q} - \frac{q}{2k}, \\ \cos \phi_{\mathbf{k}} &= \frac{v_F^{(i)2} - v_F^{(j)2}}{v_F^{(i)2}} \frac{k}{2q} - \frac{q}{2k}.\end{aligned}\tag{29}$$

Each $\Delta_{i,j}$ (or $v_F^{(i,j)}$) could independently correspond to $\Delta_>$ or $\Delta_<$, i.e., three different values are allowed. If the two gaps are identical, the result is similar to the previously used single value $\cos \phi_{\mathbf{k}} = -q/(2k)$, as shown in Fig. 7. The other presented situation is a Dirac cone with two different branches, corresponding to Fermi velocities $v_F^{(1)} \neq v_F^{(2)}$. In the limit $v_F^{(1)} \rightarrow 0$, this arrangement becomes equivalent with pseudospin-1 dice lattice, or an $\alpha - T^3$ artificial material.⁷¹

Our numerical results for the inverse relaxation time $1/\tau(\varepsilon|T)$ and the conductivity are presented in Fig. 8. The temperature-dependent conductivity increases as the temperature is raised, which is a property of an insulating system⁴⁸ Generally it happens due to the increase of the polarizability, dielectric function and screening. Consequently, the relaxation time is suppressed, as we see from Fig. 8 (a) and (b). Due to the thermal population and Dirac tail, the temperature acts in a way similar to electron doping, increasing the polarization function. However, this behavior is not universal, due to multiple scattering and resistivity mechanisms. Alternatively, the polarization function is normally decreased in the presence of an energy gap at all temperatures, showing $\simeq (1 - (\Delta_0/E_F)^2)$ dependence for $T = 0$ in the long-wavelength limit.

V. CONCLUDING REMARKS

We have carried out calculations of the transport properties, i.e., optical and Boltzmann conductivities, for doped buckled honeycomb lattices, Dirac cone structures with finite energy bandgaps, and two inequivalent energy subbands. Emphasis has been placed on the effect of finite doping, i.e., in considering extrinsic systems at arbitrary finite temperatures.

In all our calculations, the dynamical polarization function plays a key role. Once the chosen temperature is finite, the polarizability is obtained through an integral transformation of its zero-temperature limit, or directly by substituting the finite-temperature Fermi-Dirac distribution functions. In either case, knowing the exact value of the chemical potential for the considered structure at the selected temperature is necessary. This value is decreased with the temperature, but never reaches zero for a structure with an electron/hole symmetry, such as silicene. It monotonically increases with the enhanced Fermi energy, which is true for all temperatures, however this dependence is stronger when the temperature is relatively small and zero-temperature doping plays a major role.

Making use of some of known results for the polarizability, we presented analytic expressions for the optical conductivity for gapped graphene and silicene at zero, temperature as well as the high-temperature limit in graphene and intrinsic silicene. At $T = 0$, the negative peaks correspond to the double Fermi energy, independent of the gap, while the gap leads to more complicated, non-rectangular steps of the frequency dependence of $\sigma_O(\omega)$. At finite temperature, the sharp step is smoothed out. However, a discontinuity of its real part, and the negative peaks of its imaginary part survive. These components of the optical conductivity correspond to the temperature-dependence in the $q \rightarrow 0$ limit of each intraband particle-hole mode. They depend on the temperature, but this trend does not generally correlate with the finite-temperature chemical potential. Each peak has been calculated and identified. Based on these results, one can predict the signatures of the particle-hole modes and plasmon damping for possible device applications.

Lastly, we have calculated the Boltzmann conductivity in the relaxation time approximation for gapped graphene and silicene. We have extended existing semi-analytic expressions for the inverse relaxation time to finite energy bandgaps. In that case, the conductivity is reduced, but the decrease is mostly seen at low temperatures. We also developed a procedure for calculating allowable wave vectors (both magnitude and direction) when there are two inequivalent subbands. Since the corresponding transition rate depends only on the wave vector transfer, there must be one-to-one correspondence between the energy and k , so that the corresponding inverse relaxation times have to be calculated separately. Generally, the Boltzmann conductivity is increased with doping, and the temperature, since the two quantities often play similar roles due to the so-called thermal band population. We believe that all our obtained results are important for electronic applications of these innovative gapped Dirac lattices and the transport theories of condensed matter physics.

Acknowledgments

D.H. would like to thank the support from the Air Force Office of Scientific Research (AFOSR).

-
- ¹ A. K. Geim and K. S. Novoselov, *Nature materials* **6**, 183 (2007).
 - ² K. S. Novoselov, A. K. Geim, S. Morozov, D. Jiang, M. Katsnelson, I. Grigorieva, S. Dubonos, Firsov, and AA, *nature* **438**, 197 (2005).
 - ³ Y. Zhang, Y.-W. Tan, H. L. Stormer, and P. Kim, *nature* **438**, 201 (2005).
 - ⁴ C. R. Dean, A. F. Young, I. Meric, C. Lee, L. Wang, S. Sorgenfrei, K. Watanabe, T. Taniguchi, P. Kim, K. L. Shepard, et al., *Nature nanotechnology* **5**, 722 (2010).
 - ⁵ C.-C. Liu, W. Feng, and Y. Yao, *Phys. Rev. Lett.* **107**, 076802 (2011).
 - ⁶ P. Vogt, P. De Padova, C. Quaresima, J. Avila, E. Frantzeskakis, M. C. Asensio, A. Resta, B. Ealet, and G. Le Lay, *Phys. Rev. Lett.* **108**, 155501 (2012).
 - ⁷ H. Xie, T. Ouyang, É. Germaneau, G. Qin, M. Hu, and H. Bao, *Physical Review B* **93**, 075404 (2016).
 - ⁸ M. Ezawa, *New Journal of Physics* **14**, 033003 (2012).
 - ⁹ B. Aufray, A. Kara, S. Vizzini, H. Oughaddou, C. Leandri, B. Ealet, and G. Le Lay, *Applied Physics Letters* **96**, 183102 (2010).
 - ¹⁰ P. De Padova, C. Quaresima, C. Ottaviani, P. M. Sheverdyeva, P. Moras, C. Carbone, D. Topwal, B. Olivieri, A. Kara, H. Oughaddou, et al., *Applied Physics Letters* **96**, 261905 (2010).
 - ¹¹ B. Lalmi, H. Oughaddou, H. Enriquez, A. Kara, S. Vizzini, B. Ealet, and B. Aufray, *Applied Physics Letters* **97**, 223109 (2010).
 - ¹² M. Ezawa, *Phys. Rev. Lett.* **109**, 055502 (2012).
 - ¹³ C.-C. Liu, W. Feng, and Y. Yao, *Phys. Rev. Lett.* **107**, 076802 (2011).
 - ¹⁴ C. J. Tabert and E. J. Nicol, *Physical Review B* **87**, 235426 (2013).
 - ¹⁵ C. J. Tabert and E. J. Nicol, *Physical Review B* **88**, 085434 (2013).
 - ¹⁶ C. J. Tabert and E. J. Nicol, *Phys. Rev. B* **89**, 195410 (2014).
 - ¹⁷ Z. Ni, Q. Liu, K. Tang, J. Zheng, J. Zhou, R. Qin, Z. Gao, D. Yu, and J. Lu, *Nano letters* **12**, 113 (2011).
 - ¹⁸ M. Dávila, L. Xian, S. Cahangirov, A. Rubio, and G. Le Lay, *New Journal of Physics* **16**, 095002 (2014).
 - ¹⁹ L. Li, S.-z. Lu, J. Pan, Z. Qin, Y.-q. Wang, Y. Wang, G.-y. Cao, S. Du, and H.-J. Gao, *Advanced Materials* **26**, 4820 (2014).
 - ²⁰ A. Acun, L. Zhang, P. Bampoulis, M. Farmanbar, A. van Houselt, A. Rudenko, M. Lingenfelder, G. Brocks, B. Poelsema, M. Katsnelson, et al., *Journal of physics: Condensed matter* **27**, 443002 (2015).
 - ²¹ L. Zhang, P. Bampoulis, A. van Houselt, and H. J. Zandvliet, *Applied physics letters* **107**, 111605 (2015).
 - ²² L. Zhang, P. Bampoulis, A. van Houselt, and H. Zandvliet, *Applied Physics Letters* **107**, 111605 (2015).
 - ²³ L. Li, S.-z. Lu, J. Pan, Z. Qin, Y.-q. Wang, Y. Wang, G.-y. Cao, S. Du, and H.-J. Gao, *Advanced Materials* **26**, 4820 (2014).
 - ²⁴ M. Dávila, L. Xian, S. Cahangirov, A. Rubio, and G. Le Lay, *New Journal of Physics* **16**, 095002 (2014).
 - ²⁵ P. Bampoulis, L. Zhang, A. Safaei, R. Van Gastel, B. Poelsema, and H. J. W. Zandvliet, *Journal of physics: Condensed matter* **26**, 442001 (2014).
 - ²⁶ M. Derivaz, D. Dentel, R. Stephan, M.-C. Hanf, A. Mehdaoui, P. Sonnet, and C. Pirri, *Nano letters* **15**, 2510 (2015).
 - ²⁷ C. Walhout, A. Acun, L. Zhang, M. Ezawa, and H. Zandvliet, *Journal of physics: Condensed matter* **28**, 284006 (2016).
 - ²⁸ X. Wang, Y. Hong, P. K. Chan, and J. Zhang, *Nanotechnology* **28**, 255403 (2017).
 - ²⁹ A. Feyzi and R. Chegel, *The European Physical Journal B* **89**, 193 (2016).
 - ³⁰ N. Ma and D. Jena, *Physical Review X* **4**, 011043 (2014).
 - ³¹ M. Kamatagi and N. Sankeshwar, in *AIP Conference Proceedings* (2015), vol. 1665, p. 110036.
 - ³² T. Gunst, T. Markussen, K. Stokbro, and M. Brandbyge, *Physical Review B* **93**, 035414 (2016).
 - ³³ C. Xiao, D. Li, and Z. Ma, *Physical Review B* **93**, 075150 (2016).
 - ³⁴ A. Lucas, J. Crossno, K. C. Fong, P. Kim, and S. Sachdev, *Physical Review B* **93**, 075426 (2016).
 - ³⁵ Y. Liu and P. P. Ruden, *Physical Review B* **95**, 165446 (2017).
 - ³⁶ P. Borowik, J.-L. Thobel, and L. Adamowicz, *Semiconductor Science and Technology* **31**, 115004 (2016).
 - ³⁷ E. Hwang, S. Adam, and S. D. Sarma, *Physical review letters* **98**, 186806 (2007).
 - ³⁸ S. Adam, E. Hwang, and S. D. Sarma, *Physica E: Low-dimensional Systems and Nanostructures* **40**, 1022 (2008).
 - ³⁹ S. D. Sarma, S. Adam, E. Hwang, and E. Rossi, *Reviews of Modern Physics* **83**, 407 (2011).
 - ⁴⁰ K. Bolotin, K. Sikes, J. Hone, H. Stormer, and P. Kim, *Physical review letters* **101**, 096802 (2008).
 - ⁴¹ Y. M. Zuev, W. Chang, and P. Kim, *Physical Review Letters* **102**, 096807 (2009).
 - ⁴² S. D. Sarma, E. Hwang, and E. Rossi, *Physical Review B* **81**, 161407 (2010).
 - ⁴³ S. D. Sarma and E. Hwang, *Physical review letters* **83**, 164 (1999).
 - ⁴⁴ A. Iurov, G. Gumbs, D. Huang, and G. Balakrishnan, *arXiv preprint arXiv:1707.08637* (2017).
 - ⁴⁵ A. Iurov, G. Gumbs, and D. Huang, *Journal of Physics: Condensed Matter* **29**, 135602 (2017).
 - ⁴⁶ E. V. Gorbar, V. P. Gusynin, V. A. Miransky, and I. A. Shovkovy, *Phys. Rev. B* **66**, 045108 (2002).
 - ⁴⁷ V. Y. Tsaran, A. Kavokin, S. Sharapov, A. Varlamov, and V. Gusynin, *arXiv preprint arXiv:1703.08962* (2017).
 - ⁴⁸ E. H. Hwang and S. Das Sarma, *Phys. Rev. B* **79**, 165404 (2009).

- ⁴⁹ S. Das Sarma and Q. Li, Phys. Rev. B **87**, 235418 (2013).
- ⁵⁰ B. Wunsch, T. Stauber, F. Sols, and F. Guinea, New Journal of Physics **8**, 318 (2006).
- ⁵¹ P. Pyatkovskiy, Journal of Physics: Condensed Matter **21**, 025506 (2008).
- ⁵² B. Van Duppen, P. Vasilopoulos, and F. Peeters, Physical Review B **90**, 035142 (2014).
- ⁵³ P. F. Maldague, Surface Science **73**, 296 (1978).
- ⁵⁴ A. Scholz, T. Stauber, and J. Schliemann, Physical Review B **88**, 035135 (2013).
- ⁵⁵ L. Falkovsky, in *Journal of Physics: Conference Series* (IOP Publishing, 2008), vol. 129, p. 012004.
- ⁵⁶ L. A. Falkovsky, Physics-Uspekhi **51**, 887 (2008).
- ⁵⁷ L. Falkovsky and S. Pershoguba, Physical Review B **76**, 153410 (2007).
- ⁵⁸ K. F. Mak, M. Y. Sfeir, Y. Wu, C. H. Lui, J. A. Misewich, and T. F. Heinz, Phys. Rev. Lett. **101**, 196405 (2008).
- ⁵⁹ T. Stauber, N. M. R. Peres, and A. K. Geim, Phys. Rev. B **78**, 085432 (2008).
- ⁶⁰ A. Iurov, D. Huang, G. Gumbs, W. Pan, and A. Maradudin, Physical Review B **96**, 081408 (2017).
- ⁶¹ V. Gusynin and S. Sharapov, Physical Review B **73**, 245411 (2006).
- ⁶² A. Singh, K. I. Bolotin, S. Ghosh, and A. Agarwal, Physical Review B **95**, 155421 (2017).
- ⁶³ J. P. Carbotte, J. P. F. LeBlanc, and E. J. Nicol, Phys. Rev. B **85**, 201411 (2012).
- ⁶⁴ A. Scholz and J. Schliemann, Phys. Rev. B **83**, 235409 (2011).
- ⁶⁵ P. Pyatkovskiy, Journal of Physics: Condensed Matter **21**, 025506 (2008).
- ⁶⁶ A. Iurov, G. Gumbs, D. Huang, and V. Silkin, Physical Review B **93**, 035404 (2016).
- ⁶⁷ E. H. Hwang and S. Das Sarma, Phys. Rev. B **77**, 195412 (2008).
- ⁶⁸ T. Ando, Journal of the Physical Society of Japan **75**, 074716 (2006).
- ⁶⁹ O. Kibis, Physical Review B **81**, 165433 (2010).
- ⁷⁰ K. Kristinsson, O. Kibis, S. Morina, and I. Shelykh, Scientific reports **6** (2016).
- ⁷¹ J. D. Malcolm and E. J. Nicol, Physical Review B **93**, 165433 (2016).